EUROPEAN ORGANIZATION FOR NUCLEAR RESEARCH
CERN-AB DIVISION

CERN-AB-2003-004 (ABP)

Considerations on Tevatron Luminosity and Performance Fnal, November 7 - December 17, 2002

F. Zimmermann

This report contains a loose collection of studies and considerations on various limitations of Tevatron luminosity and performance. These are either analytical calculations, computer simulations, or studies based on an Offline Shot Data Analysis (OSDA) of many stores, using JAVA packages provided by P. Lebrun, S. Panacek, et al. The results of six dedicated or end-of-the-store machine studies performed during my stay at Fermilab are not included and will be published separately. Specifically, the topics we address here comprise the expected and measured luminosity, hourglass effect, dynamic beta function, beam lifetime at injection and in collision, beam losses at the start of the ramp, electron-cloud build up for uncoalesced beams and for Run-IIb, potential-well distortion, intrabeam scattering, and Touschek effect. The treatments of the various subjects strongly differ in completeness and maturity. For example, the results on intrabeam scattering and Touschek scattering look definitive, whereas studies of beam loss and lifetime have not reached a final conclusion.

Geneva, Switzerland
23 January, 2003

AB/DIV Reps

Considerations on Tevatron Luminosity and Performance FNAL, November 7 – December 17, 2002

F. Zimmermann

December 17, 2002

Abstract

This report contains a loose collection of studies and considerations on various limitations of Tevatron luminosity and performance. These are either analytical calculations, computer simulations, or studies based on an Offline Shot Data Analysis (OSDA) of many stores, using JAVA packages provided by P. Lebrun, S. Panacek, et al. The results of six dedicated or end-of-the-store machine studies performed during my stay at Fermilab are not included and will be published separately. Specifically, the topics we address here comprise the expected and measured luminosity, hourglass effect, dynamic beta function, beam lifetime at injection and in collision, beam losses at the start of the ramp, electron-cloud build up for uncoalesced beams and for Run-IIb, potential-well distortion, intrabeam scattering, and Touschek effect. The treatments of the various subjects strongly differ in completeness and maturity. For example, the results on intrabeam scattering and Touschek scattering look definitive, whereas studies of beam loss and lifetime have not reached a final conclusion.

1 Performance Limitations

The performance appears to be limited by the following identified constraints and effects:

- the available number of antiprotons; any increase in the antiproton intensity and antiproton production rate would linearly increase the luminosity; assuming an exponential decay of the luminosity and a constant production rate of antiprotons between stores, we find that the longest possible stores yield the maximum luminosity; the average luminosity is directly proportional to the luminosity lifetime;
- the bad beam lifetime on the proton helix at injection; for example, a measured lifetime of about 2 hours during 20 minutes of pbar injection implies that about 15% of the protons are lost;
- 5–15% losses at the start of the ramp for both proton and pbar beams; the origin of these losses has not been clearly identified, although the longitudinal emittance appears to matter; exploratory studies with a slower initial ramp rate would be of interest to identify the problem;
- the poor luminosity lifetime in collision, which must be due to emittance growth; optimization and independent control of proton and pbar tunes, coupling, and chromaticity should help;
- some coherent instabilities, in particular transverse, which can happen at any time of the cycle; they can be (and are) suppressed by chromaticity, dampers, coupling, and/or octupoles;
- quenches, instabilities, and beam loss at higher proton (and/or pbar) intensities; runs with some of the highest currents terminated by quenches on the ramp or during the squeeze; this problem might be aggravated as the Tevatron beam intensities are raised further in the months to come;
- possible excitation of the beam by unknown sources and so-called ghost lines in the Schottky spectrum;

- long-range beam-beam effects; these need to be better understood, and a model must be constructed that is consistent with observations and does not, e.g., predict the opposite tune shifts (the same is true for the effect of the octupoles).

I think the three primary items are antiproton production rate, luminosity lifetime, and quenches at higher beam intensity.

2 Luminosity

There are several effects which can modify the simple geometric luminosity formula. One relates to the change of beta function with longitudinal position and can reduce the luminosity, if the bunches are much longer than the interaction-point (IP) beta function (hourglass effect), another to the change of the beta function due to the collision itself (dynamic beta function). Yet another effect would be an unwanted crossing angle at the collision point.

2.1 Hourglass Effect

If proton and antiprotons bunches are of Gaussian shape with equal bunch length, the luminosity reduction from the hourglass effect is given by the factor

$$H_G = \frac{\sqrt{2}}{\sqrt{2\pi}\sigma_z}\int_{\infty}^{\infty} e^{-\frac{s^2}{\sigma_z^2}}\frac{1}{1+\frac{s^2}{\beta^{*2}}}\,ds\,. \tag{1}$$

Using the relation [1]

$$\mathrm{erf}(xy) = 1 - \frac{2x}{\pi}e^{-x^2y^2}\int_0^{\infty}\frac{e^{-t^2y^2}}{t^2+x^2}\,dt\,, \tag{2}$$

this can be rewritten as

$$H_G = \left(1-\mathrm{erf}\left(\frac{\beta^*}{\sigma_z}\right)\right)\frac{\sqrt{\pi}\beta^*}{\sigma_z}e^{\frac{\beta^{*2}}{\sigma_z^2}}\,. \tag{3}$$

If the rms bunch lengths are not the same, we have instead (with $\Sigma_z=(\sigma_{z1}^2+\sigma_{z2}^2)^{1/2}$):

$$H_G = \left(1-\mathrm{erf}\left(\frac{\sqrt{2}\beta^*}{\Sigma_z}\right)\right)\frac{\sqrt{2\pi}\beta^*\Sigma_z}{\sigma_{z1}\sigma_{z2}}e^{\frac{2\beta^{*2}}{\Sigma_z^2}}\,. \tag{4}$$

According to M. Church and P. Lebrun, the formula for the hourglass factor, Eq. (3), can be expanded as

$$H_G \approx 1.1117 - 0.62504\frac{\sigma_z}{\beta^*} + 0.19358\left(\frac{\sigma_z}{\beta^*}\right)^2 - 0.02442\left(\frac{\sigma_z}{\beta^*}\right)^3\,, \tag{5}$$

which, somewhat surprisingly, does not equal 1 in the limit of zero bunch length. In the following we have used this approximation as it was already implemented in the JAVA program package (and adding complicated mathematical functions did not look to be an easy thing to do in JAVA). Furthermore, in the later applications, we have replaced the bunch length in Eq. (5) by the geometric mean of the rms bunch lengths for the two beams. This is not strictly correct, as can be seen from the exact Eq. (4).

2.2 Dynamic Beta Function

The change in the antiproton IP beta function is given by

$$\frac{\beta}{\beta_0} = 1 - 2\pi\frac{1}{\sin 2\pi\nu}\xi_0(1+\cos(2\Delta\phi - 2\pi\nu))\,, \tag{6}$$

where β_0 is the unperturbed beta function, ξ_0 the beam-beam tune shift for one IP, and $\Delta\phi$ the phase advance between CDF and D0. This phase advance is about 7.0 (2π) for both planes (is an integer a good choice?). For the nominal tune near 0.58, the cos term is -0.88, and the relative reduction in the antiproton beta function is only 2% for a beam-beam tune shift of $\xi_0 \approx 0.012$ per interaction point. This will hardly be noticeable. Below we will ignore this effect.

2.3 Measured and Expected Bunch-by-Bunch Luminosity

Figure 1 presents an OSDA analysis of the initial luminosity loss for stores 1906–1961. The first plot shows that the measured initial luminosity agrees rather well with the luminosity value that is expected from the measured intensities, emittances, and the computed hourglass factor. Indeed the average ratio of the measured and expected luminosity is about 15% larger than 1! In the following two plots, we show this ratio as a function of bunch no. and store number. There is some variation along each train, the highest luminosity usually being reached towards the end of each train.There is no systematic trend over the number of stores. The fourth picture shows the ratio of measured and expected luminosity as a function of the product of the two beam currents. There is a small downward trend towards higher currents, perhaps statistically insignificant, or perhaps related to the beam-beam dynamics, intrabeam scattering, or wake fields. Finally, the bottom picture compares the measured and predicted hourglass effects as a function of the bunch length (the geometric mean of proton and pbar bunch lengths). The measured hourglass factor varies somewhat less with the bunch length than expected, which might partly be explained by a large error in the measured antiproton bunch length. There is a weak evidence that the hourglass, or luminosity enhancement factor, depends on the bunch current.

3 Beam Lifetime

3.1 Injection

It has been remarked that the beam lifetime at injection is well parametrized by a quasi-exponential decay of the form $\exp(-\sqrt{t/\tau})$, but not by an exponential [2]. Figure 2 shows that the quasi-exponential decay is almost indistinguishable from the decay law

$$N(t) = \frac{N(0)}{1 + 2t/\tau} \,, \tag{7}$$

which can be obtained if the loss rate is proportional to the square of the intensity:

$$\frac{dN}{dt} = -\alpha N^2 \,, \tag{8}$$

where the coefficient α is related to τ via

$$\alpha = \frac{2}{\tau N(0)} \,. \tag{9}$$

Figure 3 shows a recent measurement, which illustrates that the proton beam lifetime at injection has as an acceptable value of 17.2 hours on the central orbit, but decreases to 3.4 hr, as soon as the proton beam is moved onto the proton helix. This suggests that the bad lifetime is related either to the reduced aperture for the off-center orbit and/or to field nonlinearities and their feed-downs.

3.2 Collision

The maximum beam lifetime that we can hope for is that determined by the total luminosity L and the total cross section $\sigma_{\rm tot}$ (70 mbarn):

$$\tau_{p,\bar{p},\max} = \frac{N_{p,\bar{p}}}{2Ln_b\sigma_{\rm tot}} \,, \tag{10}$$

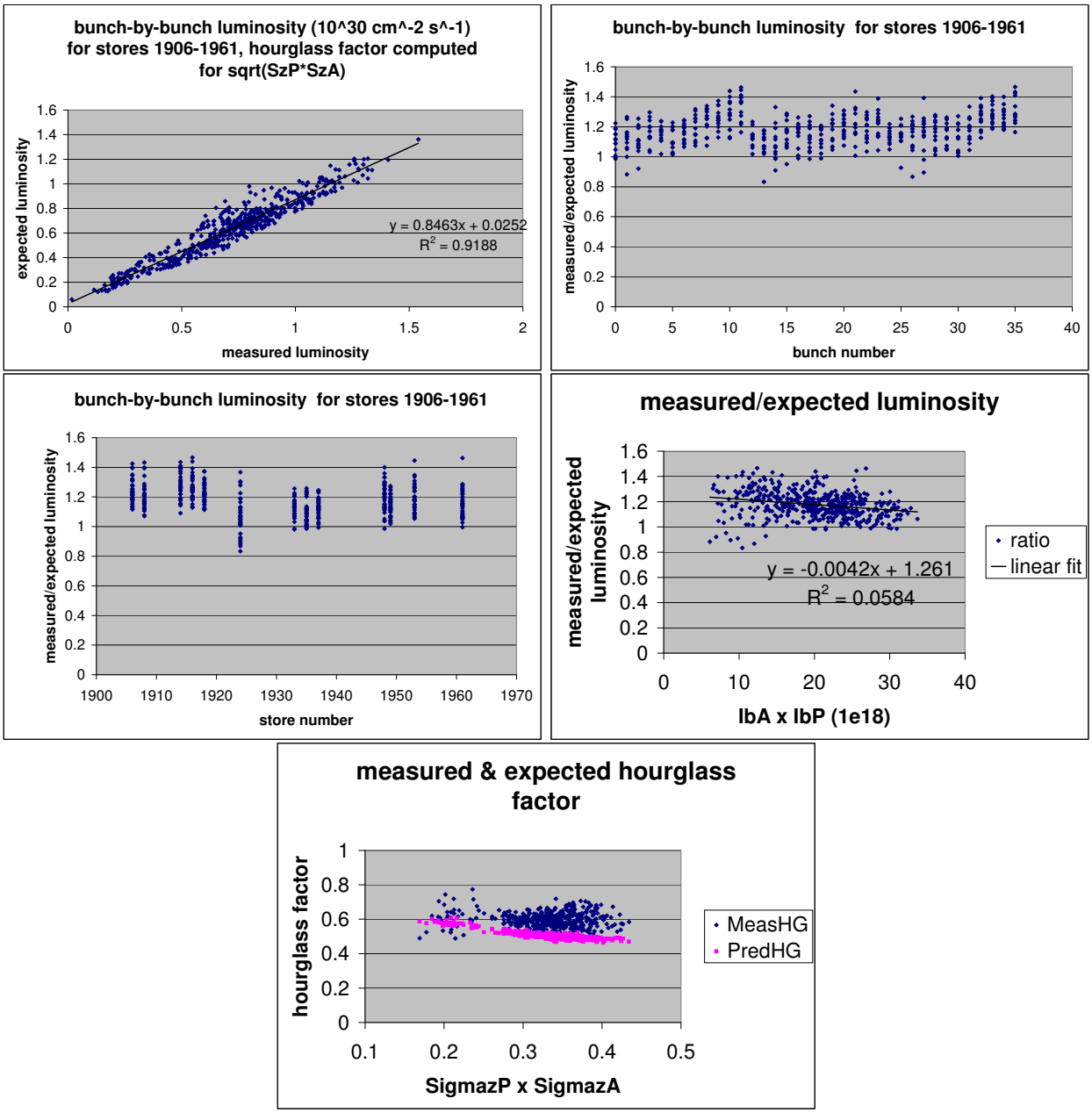

Figure 1: Various pictures illustrating the relation between measured and expected initial luminosity (top left), and its dependence on both the bunch number (top right), the store number (centre left), and the product of the beam currents (centre right). The bottom shows the measured and the expected hourglass factor as a function of bunch length. The expected luminosity was computed using the approximation of Eq. (5) and inserting for σ_z the geometric mean of the rms bunch lengths for the two beams.

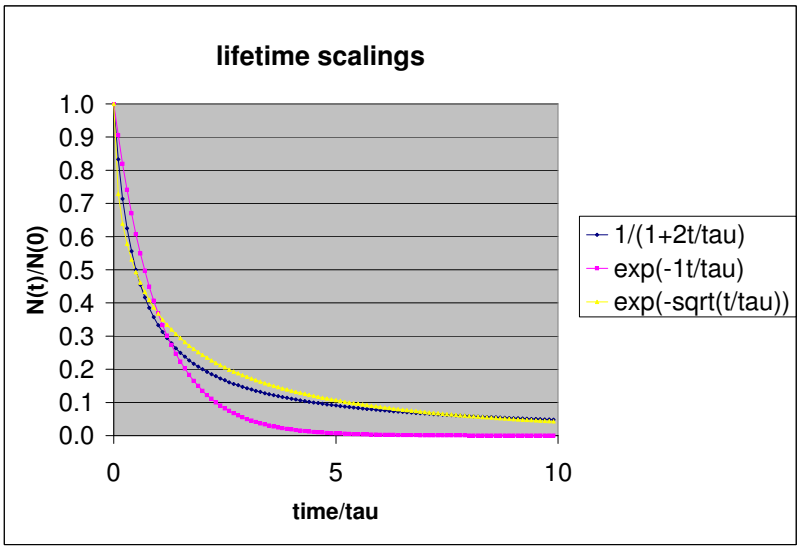

Figure 2: Comparison of exponential, quasi-exponential, and inverse polynomial ($\propto 1/(1+2t/\tau)$) current decay.

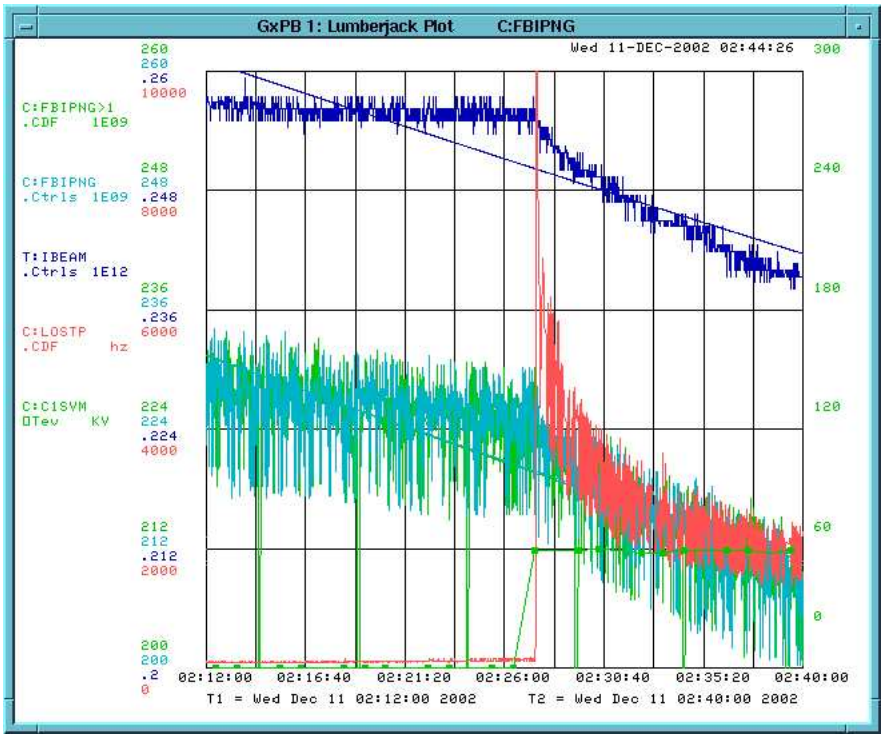

Figure 3: Measured current decay on the central orbit (left part) and on the proton helix (right part), December 12, 2002 (courtesy J. Annala, P. Ivanov, et al.).

Table 1: Fitted beam and luminosity lifetimes at 980 GeV for stores 2047 and 2049

store	2047	2049
proton lifetime τ_p	168 hr	221 hr
antiproton lifetime $\tau_{\bar{p}}$	66 hr	60 hr
luminosity lifetime τ_L	22 hr	20 hr

where the factor of 2 accounts for the two interaction regions, n_b is the number of bunches per beam, and $N_{p,\bar{p}}$ refers to the bunch population or protons or antiprotons. We have evaluated this expression for the two stores 2047 and 2049. The initial bunch intensities were $N_{\bar{p}} = 1.9 - 2.0 \times 10^{10}$ and $N_p = 1.7 - 1.9 \times 10^{11}$ (the first lower numbers correspond to store 2049), and the initial luminosities about 24×10^{30} cm^{-2}s^{-1} in either case.

Figure 4 depicts the logarithm of the beam intensity and the luminosity as a function of time over a time period of about 20 hours. The curve does not noticeably deviate from a straight line, *i.e.*, the decay is exponential. A linear fit yields the decay constants listed in Table 1.

The maximum beam lifetime according to Eq. (10) is 60 hr for the antiprotons and about 550 hr for the protons. The fitted antiproton lifetime in Table 1 agrees with the maximum possible value. This demonstrates that the initial antiproton beam lifetime is entirely explained by the proton-antiproton reactions at the collision points. On the other hand, the proton lifetime is about a third to half of the maximum value of Eq. (10), suggesting that other processes become important on this longer time scale. Finally, and most importantly, the luminosity lifetime is only 20 hr, which is a third of the ideal lifetime from the antiproton intensity decay rate. The short luminosity lifetime indicates a considerable emittance growth rate on the flat top.

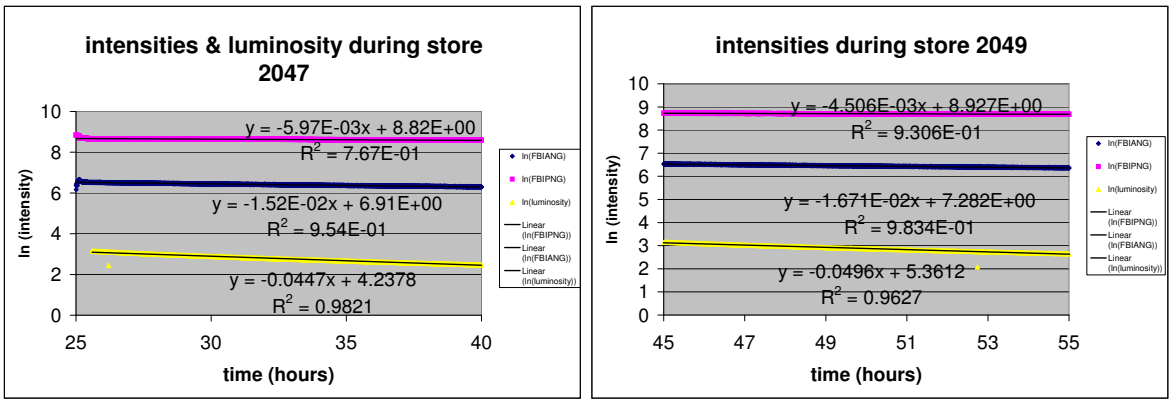

Figure 4: Logarithm of beam intensity and luminosity as a function of time and linear fit for stores 2047 (left) and 2049 (right).

This hypothesis is investigated a little further in Figure 5, which shows the beam intensities, transverse sizes, and rms bunch lengths as a function of time in collisions over about 20 hours, for store 2076. The transverse beam sizes grow slowly, the bunch length more rapidly. It is not evident if this alone can fully account for the poor luminosity lifetime.

It has been suspected, but not verified experimentally, that the poor luminosity lifetime in collision is related to the high chromaticity. One effect of the chromaticity is that it changes the phase advance from turn to turn for an off-momentum particle. This particle will thus undergo different phase advances from collision with the opposite beam to the next. This will lead to a harmonic modulation in the time of the beam-beam interaction at the synchrotron frequency, which could drive certain resonances.

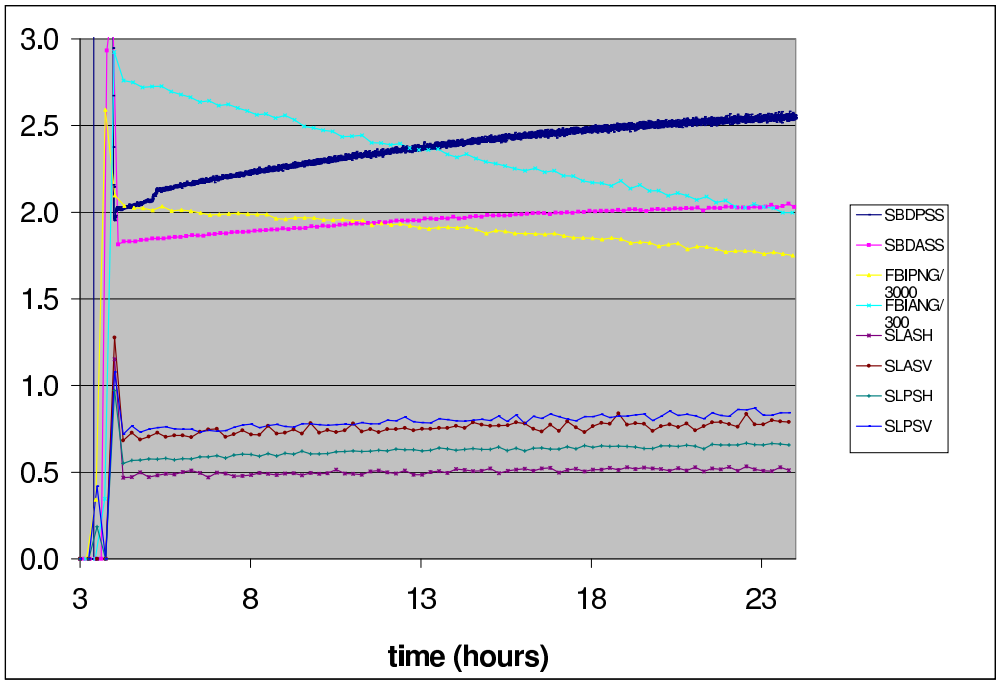

Figure 5: Intensities (FBIPNG in 3×10^{12}; FBIANG in 3×10^{11}) transverse beam sizes from synchrotron-light monitor (SLASH, SLASV, SLPSH, SLPSV; in mm), and rms bunch lengths (SBDPSS, SBDASS; in ns) for both beams as a function of time during collisions in store 2076.

For example, assuming a chromaticity $Q' \approx 5$ and considering a particle with an energy offset of $\sigma_\delta \approx 1.8 \times 10^{-4}$, the change in betatron phase advance between the collisions with the centre of the other beam on two successive turns is

$$\Delta\phi = Q' 2\pi\sigma_\delta \approx 0.006 \text{ rad} . \tag{11}$$

A similar effect arises, independently of the chromaticity, from the longitudinal motion of the particle:

$$\Delta\phi = \frac{\Delta s}{2\beta^*} = \frac{\alpha_c C \sigma_\delta}{2\beta^*} \approx -0.005 \text{ rad}. \tag{12}$$

This means that for a chromaticity of +5 these two effects almost exactly cancel each other. Therefore, it is not evident that a lower chromaticity would be better.

4 Beam Loss at the Start of the Ramp

Figure 6 illustrates the beam loss and the bunch length change which occur at the start of the ramp. The beam loss (about 6% here) happens over the first 10 seconds of the ramp. The bunch-length decrease due to adiabatic damping and/or longitudinal shaving continues monotonically over a much longer time.

We have tried to fit the measured relative proton beam loss during the ramp $\Delta N_p/N_p$ (where N_p is the proton bunch intensity at the start of HEP) as a linear combination of 20 (or more) variables, namely: (1) the proton transverse emittances and rms bunch length before the ramp (ϵ_{xp}, ϵ_{yp}, σ_{zp}), (2) the proton and antiproton bunch intensities (N_p and N_{pb}), (3) the square of all these variables and their second-order cross products ($(\Delta\epsilon_{xp})^2 \equiv (\epsilon_{xp} - \bar{\epsilon}_{xp})^2$, ($\Delta\epsilon_{yp}^2$, $\Delta\sigma_z^2$, $\Delta\epsilon_{yp}\Delta\sigma_z$, $\Delta\epsilon_{xp}\Delta\sigma_z$, $\Delta\epsilon_{xp}\Delta\epsilon_{yp}$, $\Delta\epsilon_{yp}\Delta N_p$, $\Delta\epsilon_{xp}\Delta N_p$, $\Delta\epsilon_{yp}\Delta N_p$), (4) the bunch number in the train, and (5) the three time intervals extending from the 'start of ramp' to 'HEP', from 'Pbar Injection porch' to 'start of

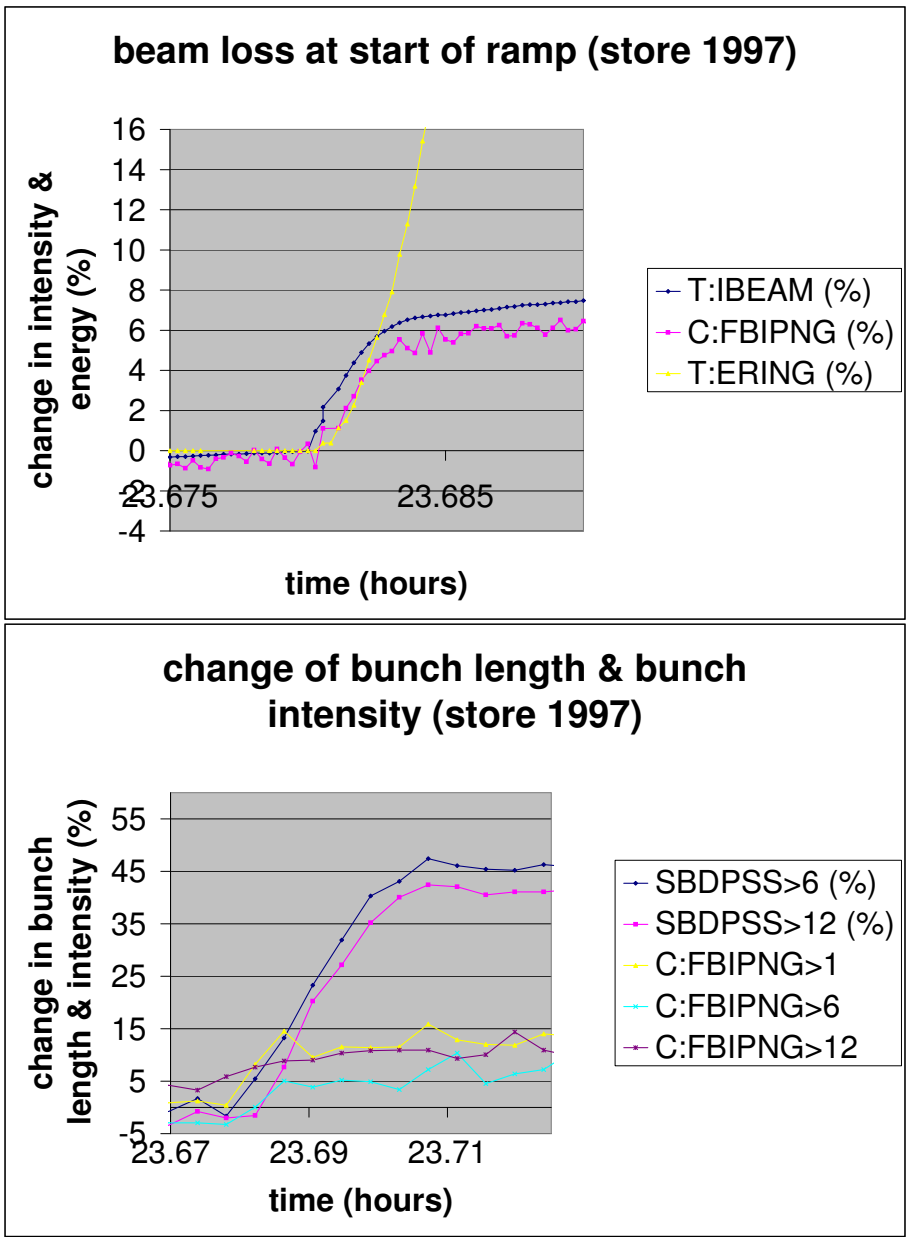

Figure 6: Relative total beam loss, bunched beam loss, and increase in beam energy as a function of time at the start of the ramp (left); relative decrease in bunch length and intensity for individual bunches (right).

ramp', and from 'Proton Injection porch' to 'start of ramp'. Optionally, sometimes higher powers or products of these variables were included as well, in an attempt to improve the fit quality.

More precisely, we tried to express the beam loss as follows:

$$\frac{\Delta N_p}{N_p}(i) = a_1\epsilon_{xp}(i)+a_2\epsilon_{yp}(i)+a_3\sigma_{zp}(i)+a_4N_p(i)+a_5N_{pb}(i)+a_6(\Delta\epsilon_{xp}(i))^2+\ldots \equiv \sum_{j=1}^{N} a_j v(i,j) \ , \quad (13)$$

where i counts the number of bunches and stores, and j the variables on the right-hand side, whose total number is N. The coefficients a_j are to be fitted. Note that from all variables on the right-hand side the average value is subtracted. If we normalize these variables to their respective rms variation, as

$$\frac{\Delta N_p}{N_p}(i) = \sum_{j=1}^{20} \tilde{a}_j \frac{v(i,j)}{\sqrt{\frac{1}{M}\sum_{i=1}^{m} v(i,j)^2 - \left(\frac{1}{M}\sum_{i=1}^{M} v(i,j)\right)^2}} \ , \quad (14)$$

the normalized fit coefficients $\tilde{a}_j$ directly reflect the relative importance of the individual variables.

Our analysis included the 36 bunches, for all the 'good' stores between store no. 1906 and no. 1997. The total number of data points is about $M \approx 1000$.

We applied two completely different algorithms to compute the fit coefficients.

The first algorithm was proposed by P. Emma and T. Lohse [4] for fitting beam trajectories. It takes into account the measurement error for the target variable $\Delta N_p/N_p$ as well as for all the independent variables on the right-hand side. The algorithm finds an optimum solution to the equation

$$\mathbf{u}^t \cdot \mathbf{z} = 0 \ , \quad (15)$$

by determining the smallest eigenvalue of the matrix

$$C_{ij} = \sum_{l=1}^{N+1} z_{li} z_{lj} \ . \quad (16)$$

The corresponding normalized eigenvalue $\mathbf{u}$ is the desired solution. Before applying this equation, all variables, including the target quantity $\Delta N_p/N_p$ on the left, are normalized, in this case not by their variation from sample to sample, but by an estimate of the respective measurement error. We have assumed errors of 1% for intensity, and 5% for the emittance and bunch length.

Unfortunately the Lohse-Emma fit did not work well for our problem. The correlation coefficient,

$$R^2 = \frac{\left[\sum_i (\Delta N_p/N_p)_{\rm pred}(i)(\Delta N_p/N_p)_{\rm meas}\right]^2}{\left[\sum_j (\Delta N_p/N_p)_{\rm pred}(j)(\Delta N_p/N_p)_{\rm pred}(j)\right]\left[\sum_k (\Delta N_p/N_p)_{\rm meas}(k)(\Delta N_p/N_p)_{\rm meas}(k)\right]} \ , \quad (17)$$

resulting from such a fit is poor for our problem, and the fit prediction differs strongly from the measured beam loss, as is illustrated in Fig. 7. Using this algorithm we obtained only $R^2 \approx 0.03$, though this value might depend on the choice of the error magnitude for the individual variables. In addition, the fit coefficients changed by orders of magnitude (including their sign) depending on how many other variables were included, and depending on the maximum order of the terms included (We considered terms up to 4th order, *e.g.*, $(\Delta\epsilon_{xp})^4$.)

A better approach turned out to be the following, based on a singular-value decomposition (SVD) [5]. We do not take into account the measurement errors and rewrite the fit equation as

$$\mathbf{n} = \mathbf{V}\mathbf{a} \ , \quad (18)$$

where $\mathbf{a}$ is the vector of *ncor* coefficients to be determined, and $\mathbf{n}$ is the huge *ndata*-component vector of beam-loss data points. The matrix $\mathbf{V}$ has *ndata* rows and *ncor* columns. It can be decomposed and inverted using SVD. That is, the matrix $\mathbf{V}$ can be expressed as

$$\mathbf{V} = \mathbf{U}\mathbf{\Lambda}\mathbf{W}^t \ , \quad (19)$$

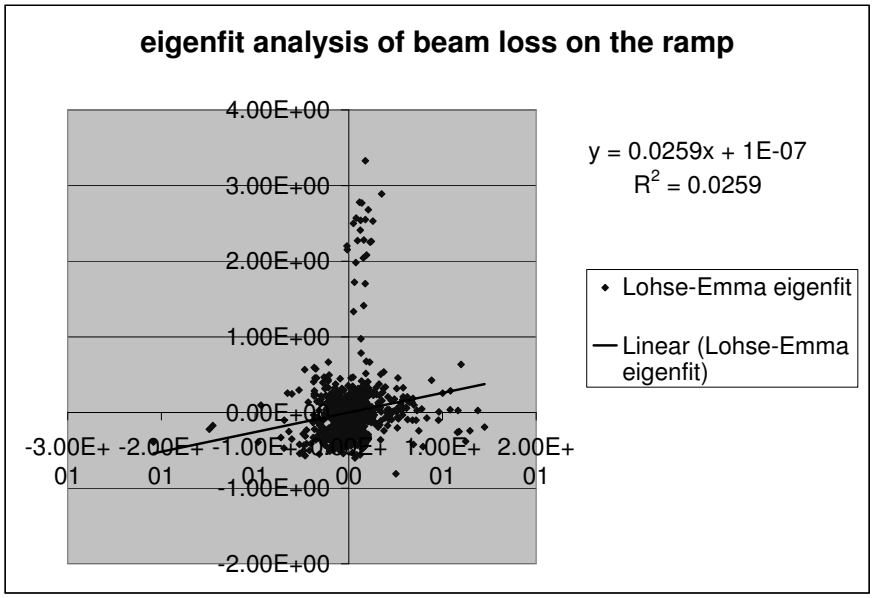

Figure 7: Measured vs. fitted relative beam loss on the ramp $\Delta N_p/N_p$, normalized to start intensity at HEP, obtained from the Lohse-Emma 'eigenfit' analysis for a certain set of error bars.

where the matrix $\mathbf{\Lambda}$ is a diagonal, and $\mathbf{U}$ and $\mathbf{W}$ are orthonormal. When inverting $\mathbf{\Lambda}$ we can set the inverse of small diagonal elements to zero, in order to avoid that degeneracies blow up the magnitude of the coefficients without sensibly contributing to the fit quality.

Figure 8 shows the dependence of the SVD fit results on the number of the largest singular values taken into account. A minimum of seven values must be included to get a reasonable squared correlation coefficient, of about 0.5. This indicates that about half of the observed variation can be related to changes in the fitted variables, and that the system has at least '7 degrees of freedom'. Figure 9 compares the measured beam losses with the fit prediction, for various numbers of singular values retained. These SVD fits appear much superior to what could be achieved with the Lohse-Emma fits, for this particular application.

Table 2 lists the normalized coefficients $\tilde{a}_j$ of Eq. (14) obtained by various fits, where all variables v_j are normalized to their rms variation, and thus the magnitude of the coefficients directly reflects the relative sensitivity. We note that the coefficients strongly vary depending on which of the two fitting algorithms is used, and, for the SVD technique, how many eigenvalues are retained. There is an indication that the beam loss is sensitive to the rms bunch length, the proton intensity, the square of the vertical emittance, the square of the bunch length, and the time between HEP and start of the ramp (the last correlation might reflect a common origin rather than a causal connection). Table 3 lists the corresponding unnormalized coefficients a_j of Eq. (13) for the two SVD fits, where the associated variables have the same units as retrieved from SDA.

5 Electron Cloud

On December 10, the emittance growth on the ramp was studied for an uncoalesced beam, by J. Annala, B. Hanna, et al. They observed that the pressure strongly increased in four of the straight sections, when the number of bunches exceeded a threshold value of about 30, and the bunch population a value of about 4×10^{10}. The observed threshold behavior of the pressure as a function of beam current is illustrated in Fig. 10.

The characteristics of the Tevatron pressure rise highly resemble the electron cloud build up due to beam-induced multipacting which has been observed since about three years in the CERN SPS,

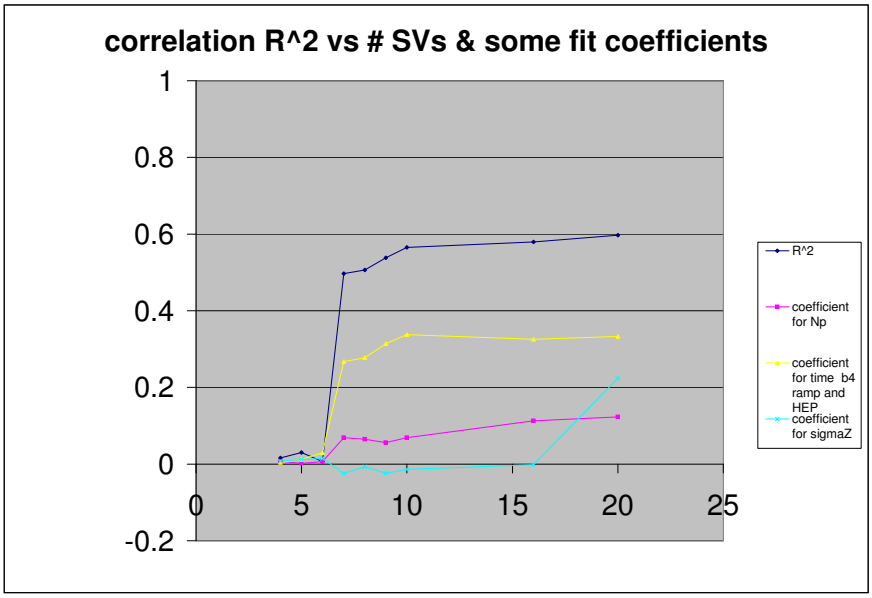

Figure 8: Correlation coefficient of fitted and measured beam loss, and fit coefficients for three variables (proton bunch intensity N_p, rms bunch length, and time interval between 'before ramp' and 'HEP' as a function of the number of singular values retained in the SVD fit.

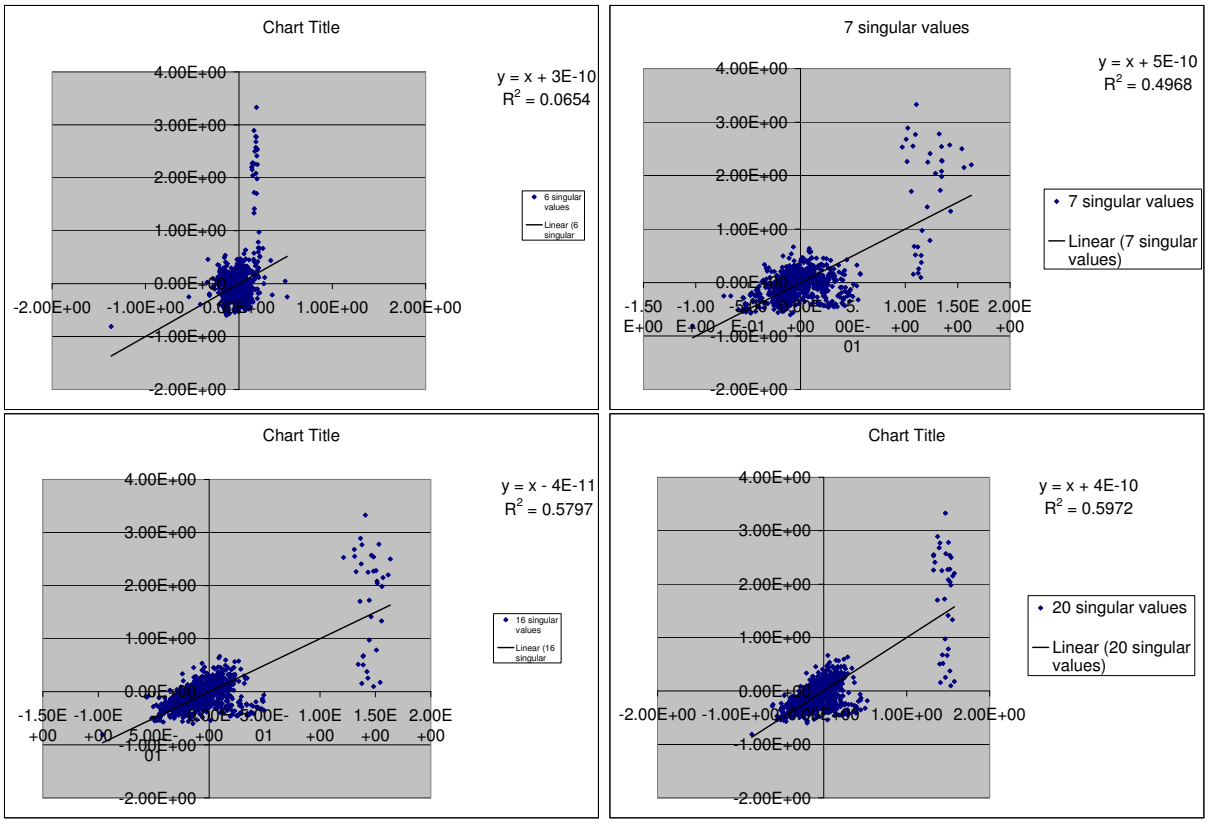

Figure 9: Measured vs. fitted relative beam loss on ramp $\Delta N_p/N_p$, normalized to start intensity at HEP, if different numbers of singular values are retained in the SVD matrix inversion.

Table 2: Fitted coefficients $\tilde{a}_j$ for the 'normalized' variables.

variable	ϵ_{xp}	ϵ_{yp}	σ_{zp}	$N_{\bar{p}}$	N_p	$\Delta\epsilon_{xp})^2$	$(\Delta\epsilon_{yp})^2$	σ_z^2	$N_{\bar{p}}^2$	N_p^2
eigenfit	0.210	−0.108	0.487	0.406	−0.393	−14.758	−4.823	−3.446	0.324	2.531
SVD (16 sing. values)	0.090	0.067	−0.001	0.066	0.113	0.002	−0.041	0.000	0.022	−0.006
SVD (20 sing. values)	0.088	0.066	0.224	0.061	0.123	0.127	0.0226	0.230	0.014	0.035
variable	$\epsilon_{yp}\sigma_{zp}$	$\epsilon_{xp}\sigma_{zp}$	$\epsilon_{xp}\epsilon_{yp}$	$\epsilon_{yp}N_p$	$\epsilon_{xp}N_p$	$\sigma_z N_p$	$i_{\rm bunch}$	$\Delta t_{\rm ramp}$	$\Delta t_{\bar{p}{\rm inj}}$	$\Delta t_{p{\rm inj}}$
eigenfit	6.466	−5.922	15.735	2.065	0.246	1.735	7.358	−0.706	−0.308	-1.122
SVD (16 sing. values)	0.012	−0.005	−0.023	0.023	−0.001	0.032	0.007	0.325	0.020	−0.066
SVD (20 sing. values)	−0.010	0.060	−0.211	−0.102	0.040	0.028	0.024	0.333	0.031	−0.054

Table 3: Fitted coefficients a_j for the unnormalized variables.

variable	ϵ_{xp}	ϵ_{yp}	σ_{zp}	$N_{\bar{p}}$	N_p	$\Delta\epsilon_{xp})^2$	$(\Delta\epsilon_{yp})^2$	σ_z^2	$N_{\bar{p}}^2$	N_p^2
SVD (16 values)	0.038	0.017	−0.003	0.001	0.006	0.000	−0.002	−0.001	0.000	0.000
SVD (20 values)	0.037	0.016	0.497	0.008	0.007	0.006	0.001	0.277	0.000	0.000
variable	$\epsilon_{yp}\sigma_{zp}$	$\epsilon_{xp}\sigma_{zp}$	$\epsilon_{xp}\epsilon_{yp}$	$\epsilon_{yp}N_p$	$\epsilon_{xp}N_p$	$\sigma_z N_p$	$i_{\rm bunch}$	$\Delta t_{\rm ramp}$	$\Delta t_{\bar{p}{\rm inj}}$	$\Delta t_{p{\rm inj}}$
SVD (16 sing. values)	0.000	0.004	−0.002	−0.001	0.000	0.002	0.001	0.001	0.000	0.000
SVD (20 sing. values)	−0.003	0.025	−0.010	−0.001	0.000	0.001	0.002	0.001	0.000	0.000

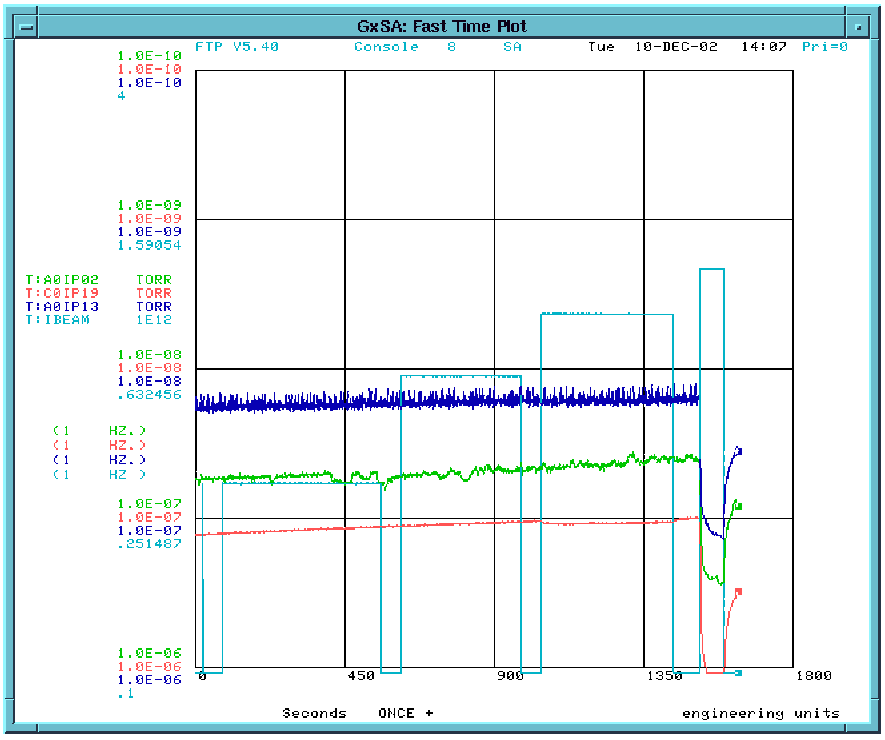

Figure 10: Measured pressure increase in several Tevatron straight sections (three of the curves) for an uncoalesced beam if the current (blue curve) exceeds a threshold, as observed on December 10, 2002 (courtesy J. Annala, B. Hanna, et al.).

Table 4: Electron-cloud simulation parameters for uncoalesced or colaesced beams.

parameter	symbol	uncoalesced	coalesced
bunch spacing	$L_{\rm sep}$	5.67 m	39.6 m
bunch population	N_b	$2-4\times10^{10}$	$2.5-3.5\times10^{11}$
rms hor. beam size	σ_x	1.5 mm	1.5 mm
rms vert. beam size	σ_y	1.0 mm	1.0 mm
rms bunch length	σ_z	0.54 m	0.54 m
number of successive bunches	n_b	40	40
max. secondary emission yield	$\delta_{\rm max}$	1.5–1.9	1.5–1.9
incident energy at maximum	$\epsilon_{\rm max}$	300 eV	300 eV
elastic electron reflection		included	included
vacuum pressure	p	10 ntorr	10 ntorr
region		dipole & field-free	field-free
chamber half aperture	$h_{x,y}$	25 or 35 mm	25 or 35 mm

as well as at many other accelerators. A recent comprehensive review of this phenomenon can be found in the proceedings of the ECLOUD'02 workshop [6].

In the Tevatron, the bunch spacing of the uncoalesced beam is 18.9 ns, and, hence, it is similar to the LHC-beam bunch spacing in the SPS. The threshold bunch current is also similar to the threshold seen in the SPS at the start of a run, prior to any conditioning. It is interesting that simultaneously with the pressure increase, also the beam Schottky power was enhanced, and a series of sudden strong excitations were seen in the tune waterfall display. Perhaps accidentally, the emittance growth during the ramp, on the central orbit, was slightly larger (by about 4πmm mrad) than the emittance growth normally obtained on the proton helix for a regular (coalesced) beam with 396-ns spacing. We might speculate that part of this additional emittance growth was due to electron-cloud induced instabilities. In the Tevatron fixed-target operation, a pressure rise was not observed. The usual number of protons for this mode of operation is 2.5×10^{13}, distributed over 83×12 bunches, or 2.5×10^{10} protons per bunch, which is below the threshold of 4×10^{10} determined here.

We ran a few computer simulations using the ECLOUD code [7], in order to verify that an electron cloud would indeed be expected to occur in the Tevatron for the beam conditions at the time of the above observations. In addition, we performed some simulations for a coalesced beam in Run-IIb conditions with 132 ns spacing. The relevant parameters assumed for either series of simulations are compiled in Table 4.

Figure 11 shows the simulated electron-cloud build up for an uncoalesced beam of 40 bunches followed by a long gap without beam. In these simulations we considered various bunch populations, two chamber radii, three different values for the maximum secondary emission yield, and either a dipole field or a field-free region. For the highest secondary emission yield, $\delta_{\rm max}=1.9$, close to that for an unconditioned surface, an electron cloud builds up in most of the cases, except for those with the lower bunch intensity $N_b=3\times10^{10}$. The simulated build up appears to be stronger in a dipole than in the regions without magnetic field. It appears that for the uncolaesced beam the build up is stronger and has a lower threshold, if the chamber radius is 25 mm, as compared with 35 mm. Though not evident in the pictures, the build up will stop due to space-charge compensation when the line density of the electrons approaches the average line density of the protons, that is the electron-line density cannot exceed the value $\lambda_e\approx N_b/L_{\rm sep}\approx7\times10^9$ m^{-1}.

Figure 12 presents simulation results for Run-II beam parameters, with 132-ns spacing and three different proton bunch intensities around $N_b=3\times10^{11}$. In this case, the threshold is lower, and the build up faster, for the chamber with the larger (35 mm) radius. This can be attributed to the much larger bunch spacing. Note that this simulation did not include the effect of the antiproton bunches.

Since the charge of the latter is much lower, this is a good first approximation. However, future more detailed simulations should include the passage of the antiproton bunches as well.

6 Potential Well Distortion

Following A. Chao and A. Hofmann [3], we consider a purely inductive wake with

$$\int_z^\infty dz' \; \rho(z') W_0'(z - z') = S\rho'(z) \; , \tag{20}$$

which corresponds to the impedance

$$Z_{||} = i\frac{S\omega}{c^2} \; , \tag{21}$$

the lengthening of a paraboblic distribution due to potential well distortion is given by the fourth oder equation:

$$\left(\frac{\hat{z}}{\hat{z}_0}\right)^4 + D\frac{\hat{z}}{\hat{z}_0} - 1 = 0 \; . \tag{22}$$

The unperturbed full bunch length is $2\hat{z}_0$. The perturbed bunch length is $2\hat{z}$. There is only one parameter D, which is proportional to the product of intensity and impedance,

$$D = -i\frac{3N_b r_p \eta c^2 c^2}{2\omega_s^2 \gamma C \omega_0 \hat{z}_0^3}\left(\frac{Z_{||}}{n}\right)\left(\frac{4\pi}{Z_0 c}\right) \; , \tag{23}$$

where, for our purposes, the slippage factor $\eta \approx \alpha_C \approx 0.0028$, and we have added a conversion factor to SI units. We can solve Eq. (22) for D or $Z_{||}/n$:

$$\left|\frac{Z_{||}}{n}\right| = \left|\frac{2\omega_s^2 \gamma C \hat{z}_0^3 \omega_0}{3N_b r_p \eta c^4}\;\frac{Z_0 c}{4\pi}\;\frac{\hat{z}_0}{\hat{z}}\left(1 - \left(\frac{\hat{z}}{\hat{z}_0}\right)^4\right)\right| \; . \tag{24}$$

At the Tevatron the momentum spread can be inferred from two horizontal wire scans with different ratio of beta functions to dispersion. The bunch length is measured by the sampled bunch display (SBD) and can be converted into an equivalent momentum spread. If bunch lengthening exists, the momentum spread estimated from the bunch length should be larger than that from the wire scans. This is indeed the case, as illustrated in Figs. 13 and 14. Figure 13 shows that, for protons, the two values of the momentum spreads are very well correlated with a systematic offset towards higher bunch lengths. Figure 14 displays the ratio of the two as a function of bunch intensity. Extrapolation to zero gives a ratio of 1.03, close to 1, as it should be. For an intensity of $N_B = 2 \times 10^{11}$ protons per bunch, the ratio is 1.16, indicating a bunch lengthening $\hat{z}/\hat{z}_0$ of about 7%.

Assuming a 7% increase in bunch length at $N_b = 2 \times 10^{11}$ with a nominal bunch length of about 0.6 m, we estimate a longitudinal impedance of 6–7 Ω, which is 2–3 times larger than the estimate of 2–3 Ω in the Run-II handbook, but still a factor of 2–3 below the predicted threshold of the longitudinal microwave instability.

7 Intrabeam Scattering

The IBS growth rate can be computed for any optics, with and without helix etc., using the MAD program, which uses the formalism developed by J. Bjorken and S. Mtingwa [8]. We multiply the growth times obtained from MAD by a factor of 2 to convert them into beam-size growth times. Then, for the proton beam parameters at injection and in collision listed in Table 5, we find the growth rates given in Table 6, using the MAD optics file *v3h01v2_new_new.lat* for 150 GeV and *v3h15av2.lat* for 980 GeV.

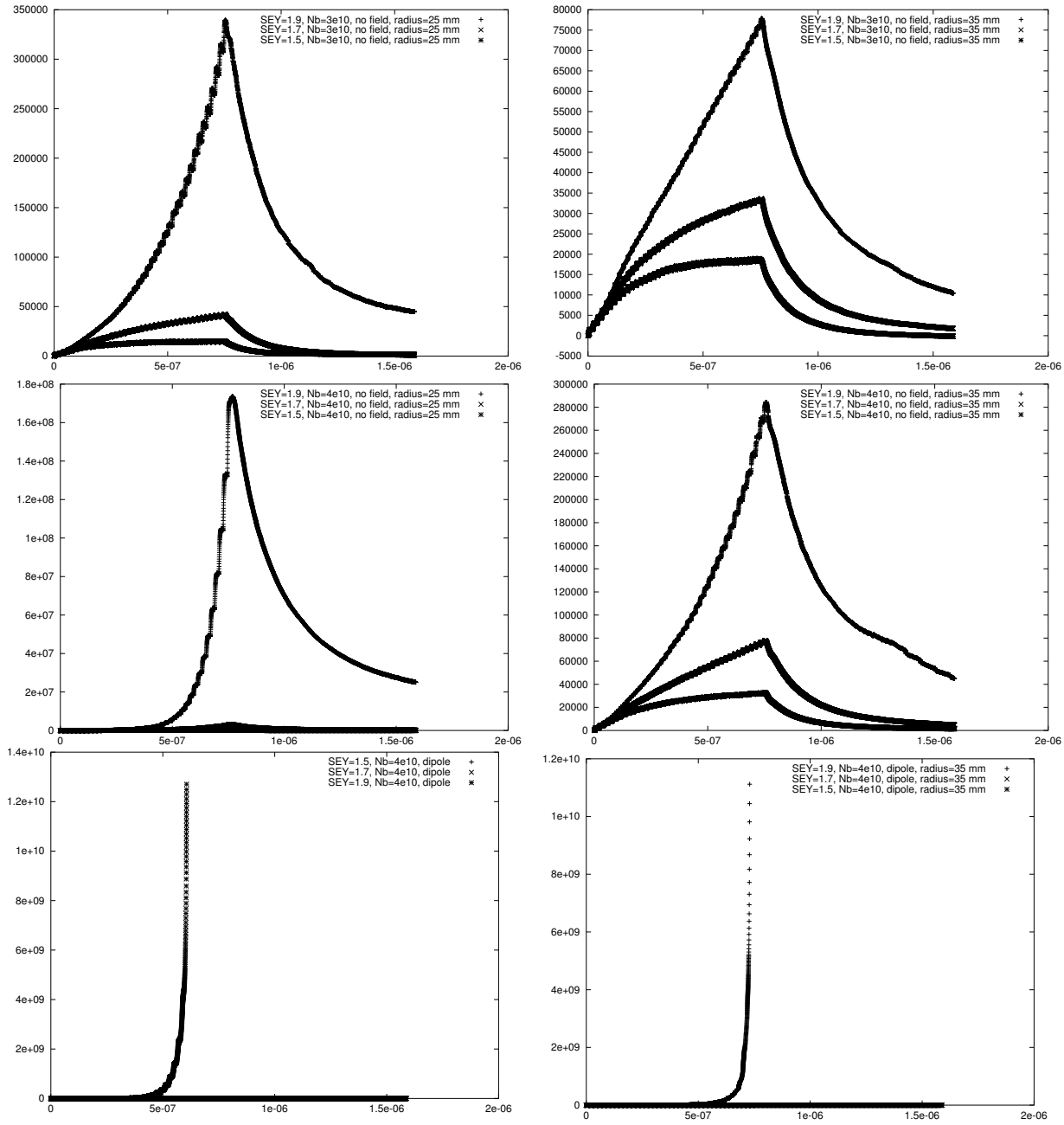

Figure 11: Simulated electron line density per meter as a function of time in seconds during the passage of 40 bunches of uncoalesced beam followed by a gap of 44 'missing bunches', for various bunch populations, fields, and maximum secondary emission yields. Top row: $N_b = 3 \times 10^{10}$ protons per bunch and field-free region, centre row: $N_b = 4 \times 10^{10}$ protons per bunch and field-free region, bottom row: $N_b = 4 \times 10^{10}$ protons per bunch and dipole; left: chamber radius 25 mm, right: chamber radius 35 mm.

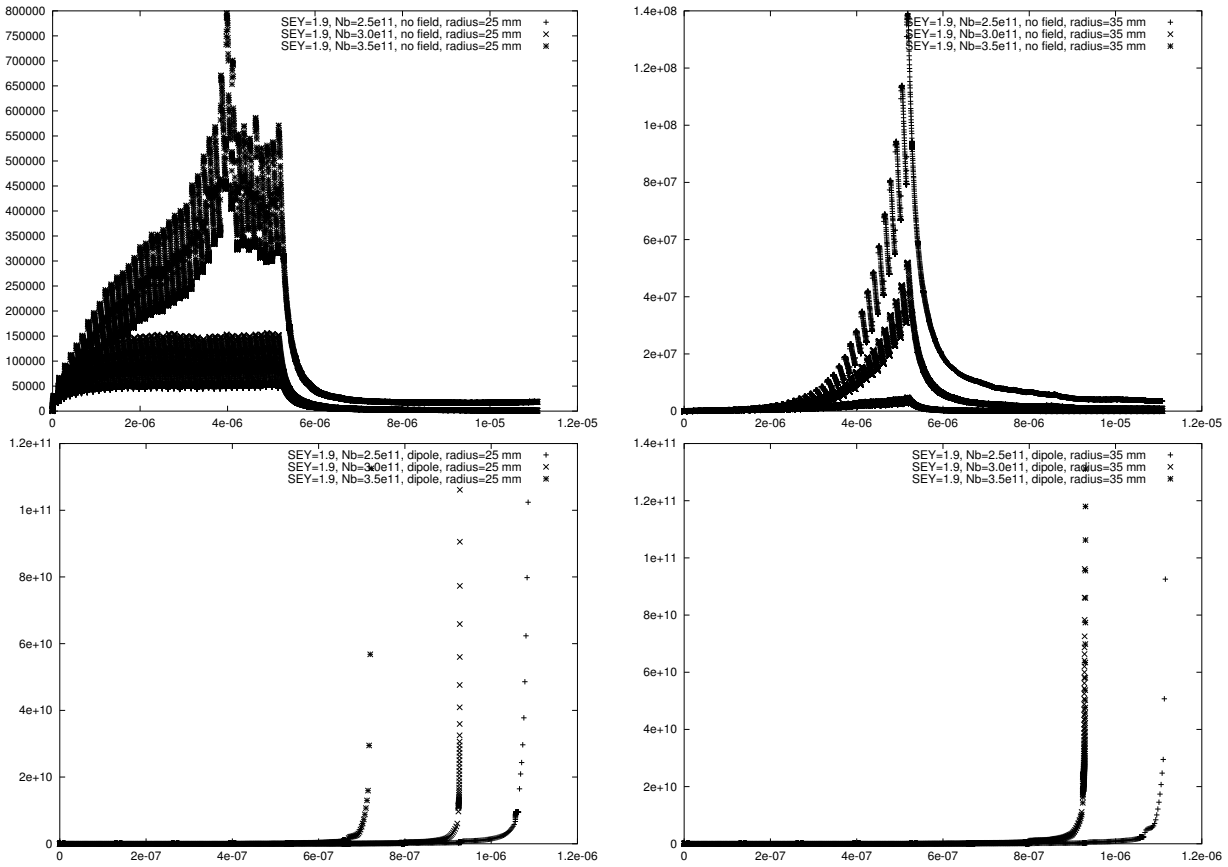

Figure 12: Simulated electron line density per meter as a function of time in seconds during the passage of 40 bunches of coalesced beam with 132 ns spacing (for Run-IIb) followed by a gap of 44 'missing bunches', for various intensities and a maximum secondary emission yield of $\delta_{\max} = 1.9$. Top row: field-free region, bottom row: dipole field; left: chamber radius 25 mm, right: chamber radius 35 mm.

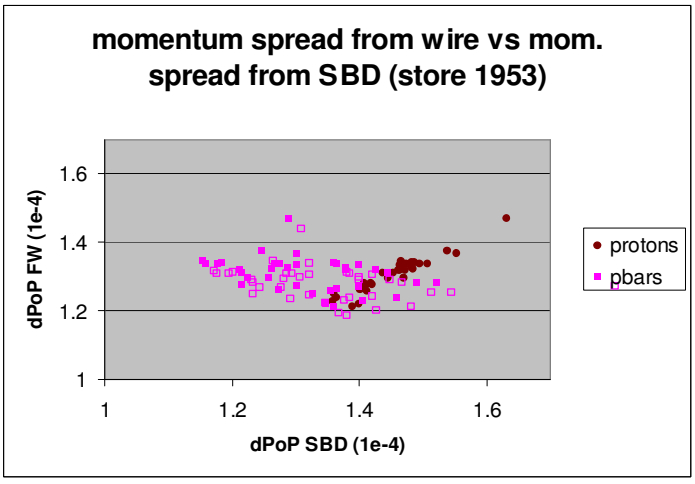

Figure 13: Momentum spread from flying wire versus momentum spread from SBD for 36 proton and antiproton bunches in store 1953.

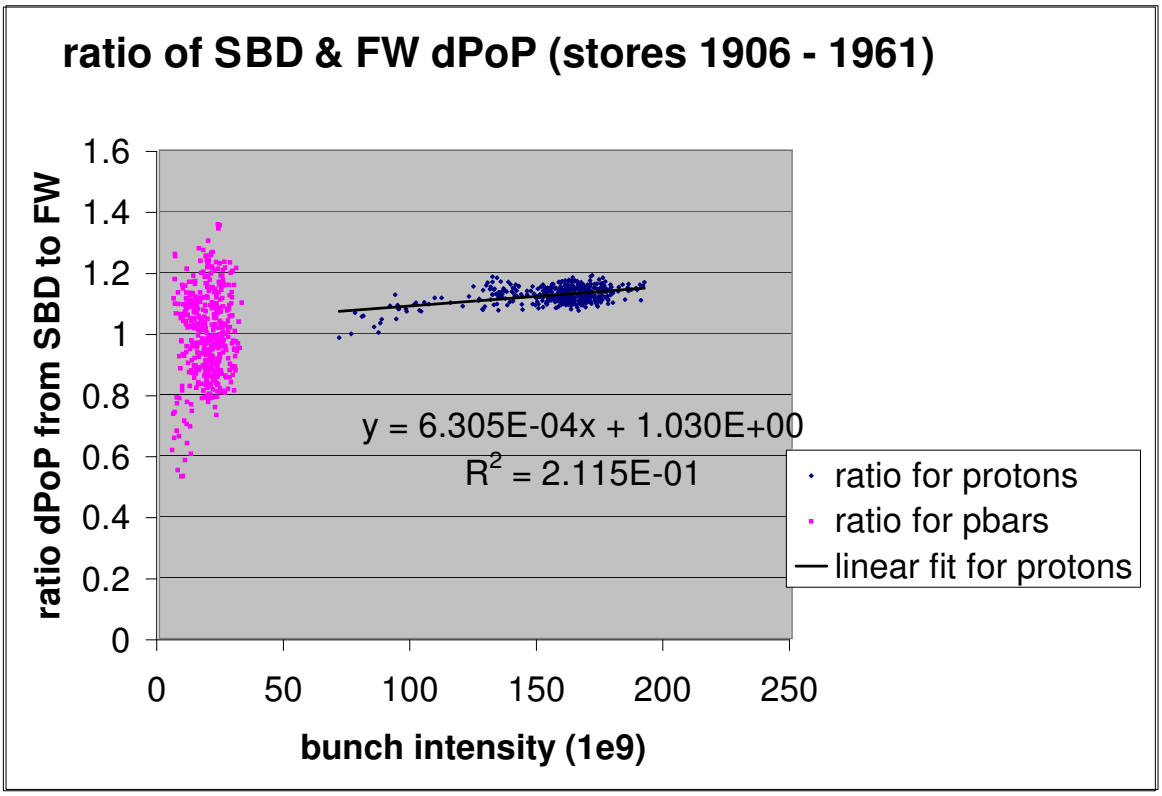

Figure 14: Ratio of the two momentum spreads, inferred from wire scanner and SBD, respectively, as a function of bunch intensity for stores 1906–1961 and a linear fit.

To gain more insight we can alternatively employ a simplified formula recently derived by K. Bane [10], which reads

$$\frac{1}{T_p} \approx \frac{r_p^2 c N (\log)}{32\gamma^3 \epsilon_x^{3/4} \epsilon_y^{3/4} \sigma_s \sigma_p^3} \left\langle \sigma_H g(a/b)(\beta_x \beta_y)^{-1/4} \right\rangle \tag{25}$$

$$\frac{1}{T_{x,y}} \approx \frac{\sigma_p^2 < \mathcal{H}_{x,y} >}{\epsilon_{x,y}} \frac{1}{T_p} \,, \tag{26}$$

where

$$a = \frac{\sigma_H}{\gamma} \sqrt{\frac{\beta_x}{\epsilon_x}} \,, \quad b = \frac{\sigma_H}{\gamma} \sqrt{\frac{\beta_y}{\epsilon_y}} \,, \tag{27}$$

$$\frac{1}{\sigma_H^2} = \frac{1}{\sigma_p^2} + \frac{\mathcal{H}_x}{\epsilon_x} + \frac{\mathcal{H}_y}{\epsilon_y} \,, \tag{28}$$

and

$$g(\alpha) \approx 2\alpha^{(0.021 - 0.044 \ln \alpha)} \,. \tag{29}$$

The angular brackets signify that the enclosed quantities, combinations of lattice and beam parameters, are averaged over the entire ring. These averages can also be extracted from the MAD program, which allows us to cross-check the MAD IBS calculations with K. Bane's approximation. Finally, we can go one step further and replace the average over products and square roots of quantities by the product and square roots of the averages, so that only the average beta function and the average dispersion invariant are needed to compute the expression.

The IBS growth rates inferred from the Tevatron optics by means of Eqs. (25) and (26) or its simplified version using average quantities are also listed in Table 6.

Table 5: Proton-Beam Parameters at Injection and Top Energy

energy	E	150 GeV	980 GeV
norm. hor. emittance (1σ)	$\gamma\epsilon_x$	3.5 μm	3.5 μm
norm. vert. emittance (1σ)	$\gamma\epsilon_y$	3.5 μm	3.5 μm
rms bunch length	σ_z	1.125 m	0.71 m
rms energy spread	σ_δ	7.3×10^{-4}	1.79×10^{-4}
bunch population	N_b	2×10^{11}	2×10^{11}
rf voltage	$V_{\rm rf}$	1 MV	1 MV
rf frequency	$f_{\rm rf}$	53 MHz	53 MHz
harmonic number	h	1113	1113
circumference	C	6283.2 m	6283.2 m
betatron tunes	$Q_{x,y}$	20.58	20.58 m
average beta function	$< \sqrt{\beta_x \beta_y} >$	56 m	65 m

An analysis by K. Bane shows that the slight disagreement between his formula and the MAD result for the Tevatron may be explained by a non-zero value of $< \zeta_x >$; namely we find $< \zeta_x > \approx 0.26$, as is illustrated in Fig. 15.

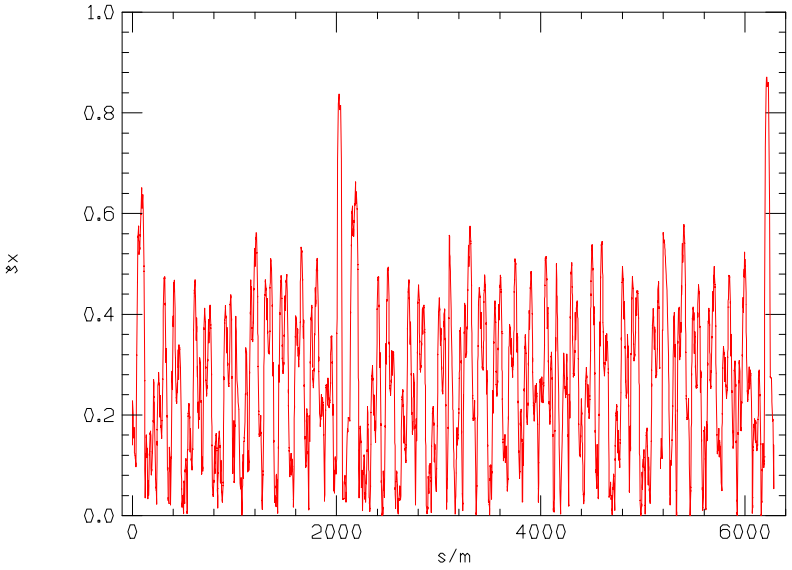

Figure 15: Plot of $\zeta_x =$ vs. longitudinal position s around the Tevatron (Courtesy Karl Bane).

The IBS growth rates for the 150-GeV case were calculated independently by Karl Bane. For the longitudinal growth time he found 200 hr using the average quantities, 169 hr averaging his formula (25) around the ring, 221 hr evaluating the Bjorken-Mtingwa expression, and 210 hr making the approximation of the SAD program, which corresponds to Eqs. (4.5)–(4.6) in the report by Bjorken-Mtingwa. Similarly, for the horizontal growth rate he obtained 47 hr using the averages, also 47 hr when using his approximation (26), 59 hr from Bjorken-Mtingwa, and 57 hr from SAD. Figure 16 compares the local growth from the full theory of Bjorken-Mtingwa with K. Bane's approximation. The differences arise primarily in the peaks of $1/\tau_{||}$ ane $1/\tau_x$.

We have verified that turning on or off the helix changes the longitudinal and horizontal growth rates computed by MAD by less than 0.5%. Hence, for the IBS calculation we can ignore vertical dispersion and betatron coupling due to the helix. We should mention though that we may have

Table 6: IBS growth times computed by the Bjorken-Mtingwa algorithm in MAD, by K. Bane's approximation, Eqs. (25) and (26) ['Bane approx.'], and by using only the average beta function and dispersion invariant ['Bane ave.'].

	injection			collision		
	MAD (B.-M.)	Bane approx.	Bane ave.	MAD (B.-M.)	Bane approx.	Bane ave.
τ_p	224 hr	178 hr	202 hr	80 hr	84 hr	98 hr
τ_x	59 hr	40 hr	49 hr	49 hr	42 hr	49 hr
τ_y	−9980 hr	4330 hr	4890	−340000 hr	15920 hr	18565

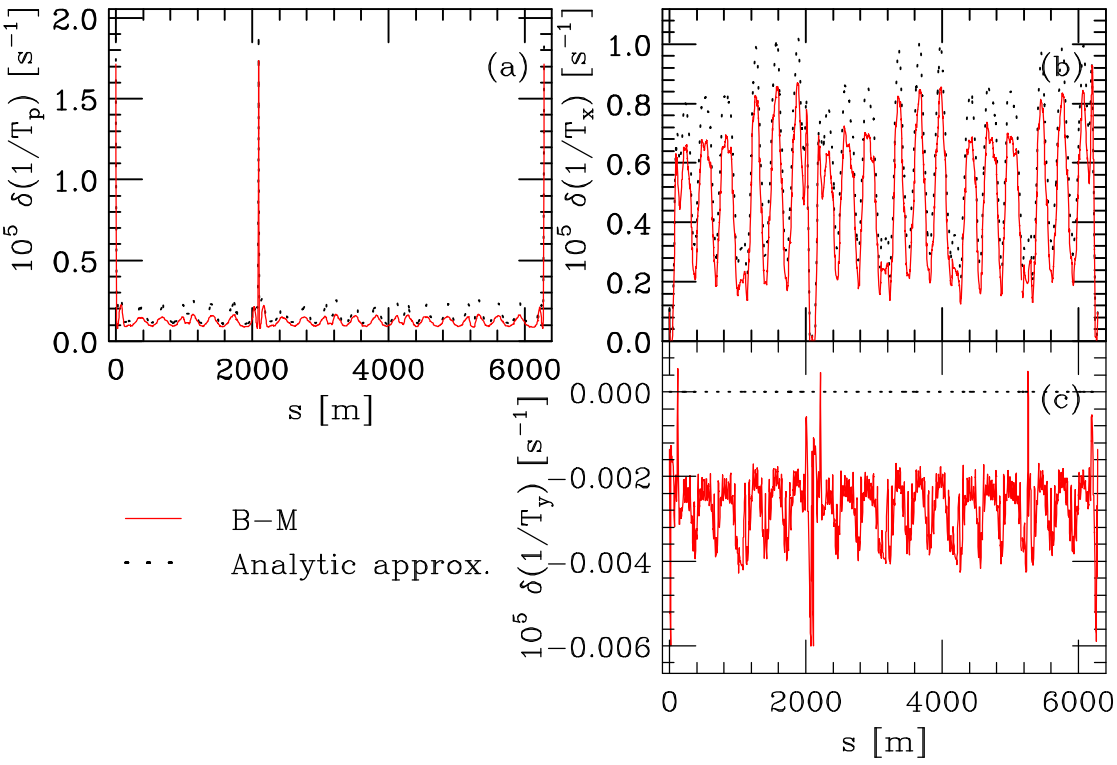

Figure 16: Local growth rates according to the Bjorken-Mtingwa theory compard with those of Eqs. (25)–(26).

some doubts whether MAD correctly takes into account the coupling, when it computes IBS rise times.

8 Touschek Scattering

This refers to single scattering events transferring particles out of the rf bucket. The loss rate from the bucket is described by

$$\frac{dN_b}{dt} = \alpha N_b^2 \ , \tag{30}$$

which, after integration, yields the amount of coasting beam as

$$N_{\rm coast} = \frac{\alpha N_0 t}{1+\alpha N_0 t} N_0 \ , \tag{31}$$

where $N_0 \equiv N(0)$ is the initial bunch population. The Touschek scattering rates for LHC and HERA were studied in Ref. [11], where we also quoted and compared formulae from various authors.

Traditionally most of the Touschek theory was developed for flat electron beam. A formula for round beams was first derived by Miyahara [12]. After correcting his result by a factor 1/2, the coefficient α is

$$\alpha = \frac{\pi r_p^2 c}{\gamma^4} \frac{\beta_x \beta_y}{\sigma_x \sigma_y V \eta} D\left(\frac{\delta q}{\eta}\right) \ , \tag{32}$$

with

$$D(\epsilon) = \sqrt{\epsilon} \int_\epsilon^\infty \frac{e^{-u}}{u^{3/2}} \left(\frac{u}{\epsilon} - 1 - \frac{1}{2}\ln\left(\frac{u}{\epsilon}\right)\right) \, du \ . \tag{33}$$

In the above expressions, $V = 8\pi^{3/2}\sigma_x\sigma_y\sigma_z$ is the bunch volume, c the speed of light, γ the energy divided by the rest mass, $\eta = (\Delta E/E)_{\rm max}$ the energy acceptance of the rf bucket, and $\delta q = \gamma\sigma_x/\beta_x$. The energy acceptance is

$$\eta \equiv \left(\frac{\Delta E}{E}\right)_{\rm max} = \left(\frac{2e}{\pi\alpha_c E_0}\frac{V_{\rm rf}}{h}\right)^{1/2} \ . \tag{34}$$

Note that a formula for arbitrary aspect ratio was derived by Piwinski [13, 14]. For a round beam it gives the same answer as Miyahara's.

Using the parameters of Table 7, we find initial Touschek lifetimes $\tau = 1/(N_0\alpha)$ of 5400 hr at injection and 4000 hr at 980 GeV. This implies that after 1 hr, the fraction of coasting beam (outside the rf bucket) is about 2×10^{-4} in either case, due to Touschek scattering alone.

Figure 17 displays an example of coasting beam measured in the Tevatron.

In order to compare this measurement with the prediction, we compute the initial and final Touschek coefficients using the beam intensity and the bunch length at the start and end of the store (initial and final intensities of 1.8×10^{11} and 1.3×10^{-11}; initial and final bunch lengths of 2.1 ns and 2.5 ns). The initial Touschek coefficient of $\alpha = 3.9 \times 10^{-19}$ s^{-1} decreases to $\alpha = 3.2 \times 10^{-19}$ s^{-1} at the end of the store. To take into account this variation of α, we may in a first approximation linearly interpolate between its initial and final value: $\alpha = \alpha_0 + \alpha_1 t$. The coasting beam is then generated at the rate

$$\frac{dN}{dt} = -(\alpha_0 + \alpha_1 t) N^2 \ , \tag{35}$$

with the solution

$$N_{\rm coast} = \frac{\alpha_0 N_0 t + \frac{1}{2}\alpha_1 t^2 N_0}{1 + \alpha_0 N_0 t + \frac{1}{2}\alpha_1 N_0 t^2} N_0 \ . \tag{36}$$

The predicted loss rate from Touschek scattering is also depicted in Fig. 17. At the beginning of the store, the Touschek scattering dominates all other beam-loss mechanisms. However, it is responsible for only a small fraction of the losses at the end of the store. In other words, the Touschek scattering

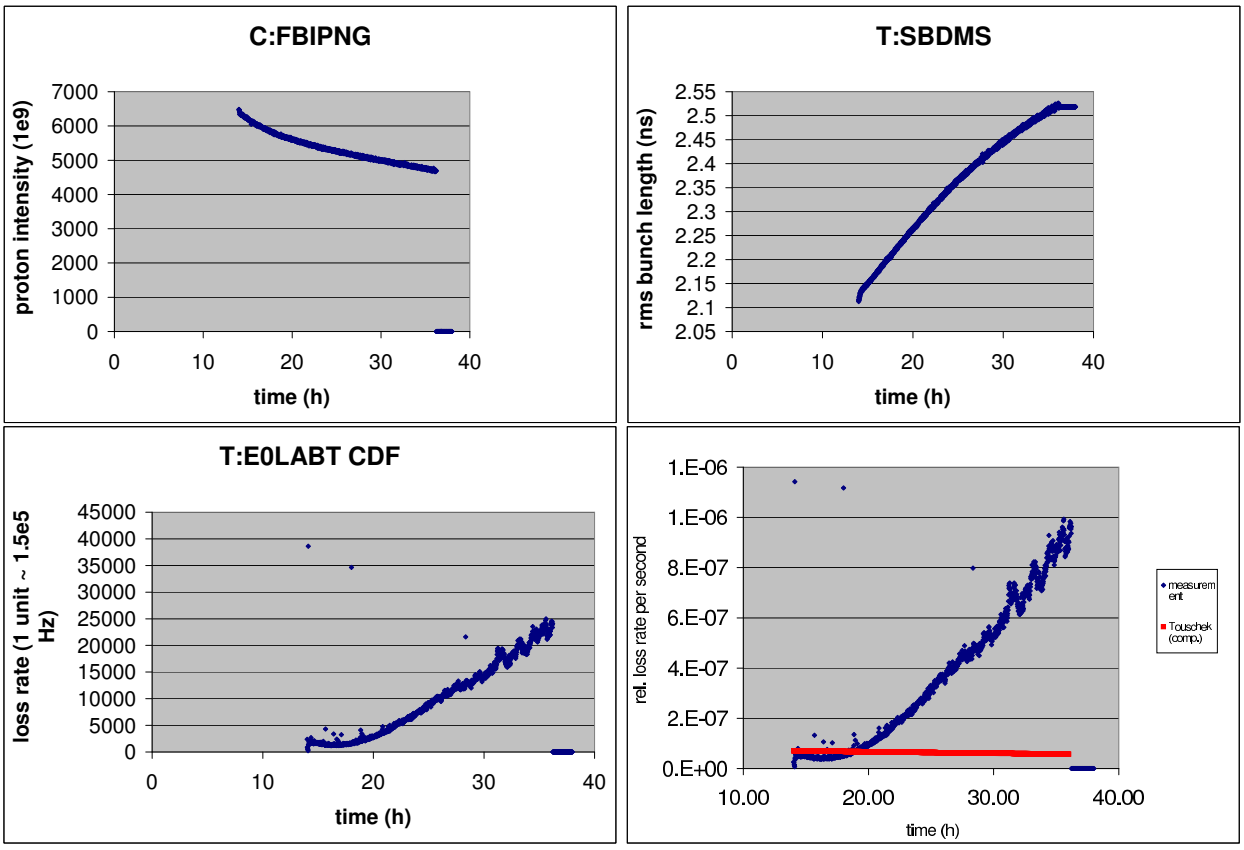

Figure 17: Example of coasting beam generation in the Tevatron for store 1955, showing the proton-bunch intensity (top left), rms bunch length (top right), local loss rate measured by CDF E0LABT (bottom left), and the total relative loss rate estimated from the measured local rate superimposed on which is the expected loss rate from Touschek scattering (bottom right), all as a function of time. The theoretical estimate assumes a ratio of 1875 between the actual total proton loss rate in Hz and the measured signal A calibration factor was determined by A. Tollestrup for a different detector (LOSTP); a comparison of the signal levels in E0LABT and LOSTP for this store yielded the conversion ratio 1875 mentioned above.

Table 7: Tevatron Parameters at Injection and Top Energy.

variable	symbol	value (inj.)	value (top)
rms horizontal beam size	σ_x	1 mm	0.4 mm
rms vertical beam size	σ_y	1 mm	0.4 mm
rms bunch length	σ_z	0.75	0.75
average beta function	$\beta_{x,y}$	49 m	49 m
momentum compaction factor	α_c	0.0028	0.0028
beam energy	E	150 GeV	980 GeV
number of protons / bunch	N_b	2×10^{11}	2×10^{11}
revolution time	T_0	21 μs	21 μs
transverse emittance	$\epsilon_{x,y}$	22 nm	3.4 nm
relativistic factor	γ	160	1045
bunch volume	V	33400 mm^3	5346 mm^3
rms uncorrel. trans. momentum in units of mc^2	δq	0.0023	0.0062
rf voltage	$V_{\rm rf}$	1 MV	1 MV
harmonic number	h	1113	1113
energy acceptance	η	1.1×10^{-3}	4.5×10^{-4}

can account for all initial losses, but it does not explain later increases in the loss rate. The latter might rather be due to intrabeam scattering or rf noise.

We have not yet examined how the theory developed by Miyahara and Piwinski should be modified when the beam fills the entire rf bucket.

Acknowledgements

I am grateful to V. Shiltsev for providing the possibility to visit the Tevatron, for his continued encouragement, and for posing many interesting challenges, to P. Lebrun for arranging a computer during my stay, and to both him and S. Panacek for patiently introducing me to the new world of JAVA and to the offline shot data analysis (OSDA), and for answering my many questions. I would also like to thank the many other colleagues at Fermilab with whom I had the pleasure to work with and from whom I learnt, notably J. Annala, P. Bauer, W. Chou, C. Darve, K. Desler, D. Edwards, W. Foster, P. Ivanov, V. Lebedev, M. Martens, R. Moore, D. Poll, K. Seiya-Koba, T. Sen, J. Slaughter, D. Still, C.Y. Tan, A. Tollestrup, A. Xiao, M. Xiao, and X.L. Zhang. Last, not least, I am grateful to K. Bane for his great help in comparing and understanding Tevatron IBS calculations.

References

[1] I.S. Gradshtein & I.M. Rhyzik, Tables of Series, Products, and Integrals, Academic Press (1995) formula (8.252.4).

[2] V. Lebedev, V. Shiltsev, private communication (2002).

[3] A. Chao, Physics of Collective Beam Instabilities in High Energy Accelerators, Wiley (1993); A. Hofmann, Fronties of Particle Beams, Lecture Notes in Physics 296, Springer-Verlag (1986), p. 99.

[4] P. Emma and T. Lohse, 'Linear Fitting of BPM Orbits and Lattice Parameters,' SLAC-CN-371 (1989).

[5] W. Press et al., 'Numerical recipes in FORTRAN : the Art of Scientific Computing', Cambridge, Cambridge Univ. Press (1992).

[6] Proceedings of ECLOUD02, Geneva, CERN Report CERN-2002-001, *http://wwwslap.cern.ch-/collective/ecloud02/proceedings/index.html* (2002).

[7] G. Rumolo and F. Zimmermann, 'Practical User Guide for ECloud,' CERN SL-Note-2002-016 AP (2002).

[8] J.D. Bjorken, S.K. Mtingwa, Part. Acc. 13, 115 (1983).

[9] K. Bane, SLAC-AP-141 (2002).

[10] K. Bane et al., PRST-AB 5, 084403 (2002).

[11] F. Zimmermann, M.-P. Zorzano, LHC Project Note 244 (2000).

[12] Y. Miyahara, Jap. J. Appl. Phys., vol. 24, p. L742 (1985).

[13] A. Piwinski, DESY 98-179 (1998).

[14] A. Piwinski, "Touschek Scattering and Intrabeam Scattering," in A. Chao and M. Tigner (eds.), "Handbook of Accelerator Physics and Engineering," World Scientific (1999).